

# A Geometric Unification of Generative AI with Manifold-Probabilistic Projection Models

Leah Bar<sup>1</sup>, Liron Mor Yosef<sup>1</sup>, Shai Zucker<sup>1</sup>, Neta Shoham<sup>1</sup>, Inbar Seroussi<sup>1</sup>, Nir Sochen<sup>1</sup>

<sup>1</sup>Department of Applied Mathematics, Tel Aviv University, Tel Aviv, Israel

{lm2, shaizucker}@mail.tau.ac.il, {barleah.libra, shohamme}@gmail.com,  
{inbarser, sochen}@tauex.tau.ac.il

January 16, 2026

## Abstract

Most models of generative AI for images assume that images are inherently low-dimensional objects embedded within a high-dimensional space. Additionally, it is often implicitly assumed that thematic image datasets form smooth or piecewise smooth manifolds. Common approaches overlook the geometric structure and focus solely on probabilistic methods, approximating the probability distribution through universal approximation techniques such as the kernel method. In some generative models the low dimensional nature of the data manifest itself by the introduction of a lower dimensional latent space. Yet, the probability distribution in the latent or the manifold’s coordinate space is considered uninteresting and is predefined or considered uniform. In this study, we address the problem of Blind Image Denoising (BID), and to some extent, the problem of generating images from noise by unifying geometric and probabilistic perspectives. We introduce a novel framework that improves upon existing probabilistic approaches by incorporating geometric assumptions that enable the effective use of kernel-based probabilistic methods. Furthermore, the proposed framework extends prior geometric approaches by combining explicit and implicit manifold descriptions through the introduction of a distance function. The resulting framework demystifies diffusion models by interpreting them as a projection mechanism onto the manifold of “good images”. This interpretation leads to the construction of a new deterministic model, the Manifold-Probabilistic Projection Model (MPPM), which operates in both the representation (pixel) space and the latent space. We demonstrate that the Latent MPPM (LMPPM) outperforms the Latent Diffusion Model (LDM) across various datasets, achieving superior results in terms of image restoration and generation.

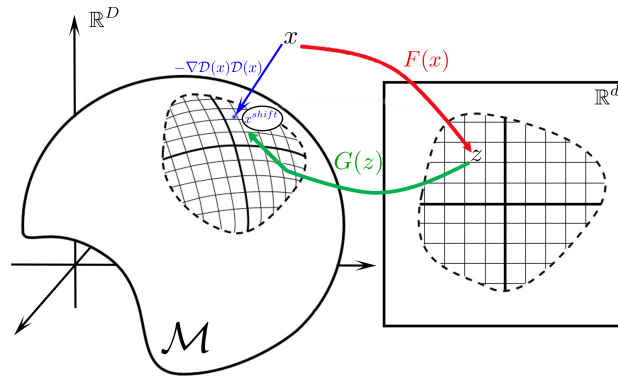


Figure 1: Illustration of our manifold-aware restoration approach. The blue path shows direct projection onto manifold  $\mathcal{M}$  using distance function  $\mathcal{D}_{\mathcal{M}}(x)$ , while the red-green path represents encoding-decoding through latent space  $\mathbb{R}^d$  via functions  $F$  and  $G$ . Ideally, both paths converge to the same manifold point, ensuring geometrically consistent restoration.

# 1 Introduction

Restoration of images refers to the inverse process of generating a clean, meaningful, and non-corrupted image from a noisy, blurred, or other degraded input. A critical aspect of this process involves the use of prior knowledge or a well-approximated distribution function over the set of clean images within a specific class. In this work, we propose the manifold assumption, which asserts that the set of desired images resides on a low-dimensional smooth manifold. We integrate this assumption with a probabilistic perspective. Specifically, we extend the conventional Monge patch description of the data manifold, typically provided by generative models such as autoencoders (AE) [24], variational autoencoders (VAE) [12], and generative adversarial networks (GAN) [6]. Our approach augments this description by introducing a distance function that assigns, for each point in the pixel (ambient/representation) space, the distance to the closest point on the manifold. We treat here images as primary examples, but evidently it can be applied to any dataset that has this manifold structure. Next, we establish a connection between the geometric framework and the probabilistic perspective by introducing a geometric-based probability function on the ambient space that is related naturally via the distance to points on the manifold to the probability distribution of data on the manifold. The latter is approximated on the latent space by kernel-based method and is pushed forward to the manifold via the generator. We further relate these approaches to diffusion-like methods, utilizing the score function to generate, in the ambient space, a vector field that directs each noisy or corrupted image towards a point on the manifold of clean images. The direction is a trade off between closeness to the corrupted image and points of higher probability on the manifold. By iteratively following this vector field, a diffusion-like flow is generated, guiding the corrupted image progressively towards a clean image residing on the manifold.

The introduction of the distance function that implicitly describe the manifold and the integration of geometric principles on the ambient space with the kernel method in the latent space constitute the primary novelties of our approach. Furthermore, we extend these general concepts, the distance function, score, and diffusion-like flow, to operate within the latent space, thereby reducing computational complexity and enhancing the accuracy of the distance function. We evaluated our proposed method on the MNIST, SCUT-FBP5500 and CelebA-HQ-256 datasets, demonstrating superior performance compared to a leading method such as the Latent Diffusion Model (LDM) [22] and DiffBir [15].

## 1.1 Related Work

In recent years, the task of generating samples from a distribution that characterizes a specific dataset or target image has emerged as a critical challenge in machine learning. This problem has been extensively studied, with solutions primarily leveraging neural networks within deep learning frameworks. Many contemporary generative models operate under the implicit assumption that datasets comprise low-dimensional objects embedded within a high-dimensional space. However, the underlying geometry of the dataset is not always explicitly considered. For instance, autoencoders (AE) [24], variational autoencoders (VAEs) [12] and Generative Adversarial Networks (GANs) [6] construct a functional mapping from the low-dimensional latent space to the high-dimensional pixel space. This functional mapping can be interpreted as a transformation from the manifold coordinate system to the pixel coordinate system. More recent approaches, such as diffusion models [26, 8], adopt a more implicit perspective on manifold structure. Geometrically, these models can be viewed as learning a directional field that guides noisy points back to the data manifold, enabling iterative projection. The diffusion process gradually transforms random noise into realistic samples by iteratively denoising along paths that converge onto the data manifold.

A central concept in many of these generative approaches is the Manifold Hypothesis [17], which posits that real-world high-dimensional data, such as images, often concentrates near a low-dimensional manifold embedded within the ambient space. This geometric perspective provides a powerful conceptual framework for understanding generative models and has significantly influenced the design of numerous architectures and training objectives. Various other manifold-aware generative approaches have been proposed. Some methods explicitly model data as residing on specific manifolds. For instance, hyperspherical VAEs [3] and hyperbolic VAEs [18] adapt generative models to handle data that naturally lies on non-Euclidean manifolds. Riemannian flow models [5, 19] incorporate Riemannian metrics into flow-based models to explicitly account for the intrinsic geometry of the data manifold. Yet, in these flows the latent space is taken the size of the ambient space ignoring the Manifold hypothesis that the dimension of the manifold is much smaller than the dimension of the ambient space. The relationship between manifold structure and probabilistic frameworks remains an active area of research. Normalizing flows [21] can be interpreted as learning diffeomorphisms between the data manifold and a simple base distribution. Score-based generative models [27] utilize the score function (the gradient of the log-density) to characterize

the data distribution, establishing a direct connection to the geometry of the data manifold. Recent works on denoising diffusion models [9] can also be interpreted as learning a vector field that guides noisy samples back to the data manifold. Despite these advancements, there remains a gap in unifying the geometric and probabilistic perspectives in generative modeling. In particular the relations between the probability distribution in the ambient space, the probability distribution on the manifold and time/noise conditioning free diffusion like flow that is coherent with the above probability distributions and the structure of the manifold are still missing.

This work addresses this gap by providing a geometric interpretation of autoencoders, leveraging geometric properties of the data, specifically the distance function to the manifold. We propose a new generative model that synthesizes both geometric and probabilistic approaches, leading to improved performance in generating high-quality samples. Our approach is based on the premise that the data manifold can be represented as a low-dimensional submanifold embedded within a high-dimensional space. We simultaneously learn both the distance function to this manifold and the probability distribution on it.

## 1.2 Image Generation/Denoising as Projection

Any corrupted image is represented by a point in the ambient space that does *not* lie on the manifold. Once a distance function is available, any such corrupted image can be projected to the nearest point on the manifold. Alternatively, we can use the inverse of the distance function’s gradient as a unit vector field in the ambient space. This unit vector field points at each point in the ambient space towards the nearest point on the manifold. By iteratively taking small steps in the direction of this negative distance gradient vector field, one obtains a process that resembles a diffusion-like model. Indeed, from a geometric perspective, the noise learning process of diffusion models aims to create a vector field in the ambient space which guides from a noisy or corrupted image toward the manifold of clean and meaningful images much like our distance gradient.

This work unifies explicit and implicit manifold representations as the foundation of a generative image model. Specifically, we incorporate geometric constraints into a loss function that jointly trains a Monge patch Decoder/Generator  $G$  and an extended encoder  $F$  that operates *throughout* the ambient space - similar in spirit to a denoising autoencoder (DAE) [29]. Although individual components of our algorithm are built on established architectures, the key contribution of our approach lies in the geometric perspective and the integration of the DAE framework with the learning of the distance function to the manifold. The three networks - Encoder  $F$ , Decoder/Generator  $G$ , and distance function  $\mathcal{D}_{\mathcal{M}}$ , are tightly coupled through the loss formulation, which is defined by the learned distance to the manifold.

# 2 Background and Theoretical Framework

## 2.1 Geometry: Manifold Hypothesis - Explicit

Many generative networks assume that images lie on a lower-dimensional manifold defined according to the latent space representation, which is embedded within a higher-dimensional representation space, such as the pixel space or ambient space. This manifold is explicitly modeled by the decoder in autoencoders (AEs) and variational autoencoders (VAEs), and by the generator in various Generative Adversarial Network (GAN) architectures. In all of these models, the manifold  $\mathcal{M}$  is represented as a Monge patch. Let the latent space be  $d$ -dimensional, parameterized by  $z$ , and the pixel space be  $D$ -dimensional, parameterized by  $x$ , that is (see Fig. 1):

$$G(z) = (x_1(z_1, \dots, z_d), \dots, x_D(z_1, \dots, z_d)).$$

In simple terms, the value at each pixel in the image (or in similar manifold-structured data) is a function of the  $d$  parameters  $z$ . In this work we use an autoencoder (or Denoising AE) where the encoder  $F(x)$  maps an image  $x \in \mathbb{R}^D$  to a point  $z \in \mathbb{R}^d$ . The generator  $G$  is as above and is used as the map that defines the manifold.

Many works, in the context of deep learning, use this representation to analyze the data set as a Riemannian manifold. We will mention here, as examples, [25, 30] where geodesics and directions of meaningful changes on the manifold are studied. In [1] the relation of the induced metric of the manifold was found to be approximated close enough to the encoded point of a clean image by the inverse covariance found in VAE.

## 2.2 Geometry: Distance Function - Implicit

Another (implicit) way to describe a manifold is as the zero level set of a function. The distance function to the manifold in the ambient (representation) space is well suited for this purpose and is defined as follows:

$$\mathcal{D}_{\mathcal{M}}(x) = \min_{y \in \mathcal{M}} \|x - y\|, \quad (1)$$

where  $\|\cdot\|$  denotes the Euclidean norm. In this high-dimensional representation space, the distance function provides a natural measure of the proximity of a point to the manifold. It is well known that  $\mathcal{D}_{\mathcal{M}}$  satisfies the Eikonal equation [7]  $\|\nabla \mathcal{D}_{\mathcal{M}}(x)\| = 1$ , with the natural boundary condition  $\mathcal{D}_{\mathcal{M}}(x) = 0$  for all  $x \in \mathcal{M}$ . Moreover, it is clear that  $-\nabla \mathcal{D}_{\mathcal{M}}(x)$  defines a vector field pointing in the direction of the shortest path to the manifold.

## 2.3 Probability: Ambient Space

On the probabilistic side, we follow works such as [10] and [28]. We begin by assuming a non-trivial distribution of clean data, denoted by  $P_c(x)$ , from which we have access to many samples namely, our dataset. We argue that for both Blind Image Denoising (BID) and image generation, the exact probability distribution is neither well-defined nor necessary. Indeed, we are not interested in the “true” probability of points outside the data manifold, i.e., degraded images. Rather, our goal is to construct a vector field that points from such degraded images toward the data manifold.

This objective can be achieved by defining a probability function that decreases monotonically with the distance from the manifold. More precisely, the probability assigned to a non-data point  $x$  is defined so that the resulting score vector field points toward the data manifold and its more densely populated regions. To this end, we naturally define the conditional probability of a corrupted image  $x$  given a clean image  $x'$  as

$$P(x | x') = f(d(x, x')),$$

where  $d(x, x')$  denotes the distance between the clean and corrupted images, and  $f$  is a monotonically decreasing function.

For ease of analysis and computation, we choose  $f$  to be Gaussian. This choice is not meant to suggest that the Gaussian is the “true” underlying function, but rather that it is sufficient for producing the desired vector field. As a second standard assumption, we take  $d(x, x') = \|x - x'\|$ . These considerations lead to the following expression for the conditional probability:

$$P_{\sigma}(x | x') = \frac{1}{Q_d} \exp\left(-\frac{\|x - x'\|^2}{2\sigma^2}\right), \quad (2)$$

where  $Q_d$  is the appropriate normalization constant.

The resulting probability distribution over the ambient space is then given by the well-known expression [10, 28]:

$$P(x; \sigma) = \int_{\mathbb{R}^D} P_{\sigma}(x | x'), P_c(x'), dx' = \frac{1}{Q_d} \int_{\mathbb{R}^D} \exp\left(-\frac{\|x - x'\|^2}{2\sigma^2}\right) P_c(x') dx', \quad (3)$$

where  $P_c(x')$  denotes the probability density of clean images.

Although the Gaussian form may appear to impose a restriction to Gaussian noise, this formulation makes no explicit assumptions about the degradation process that maps  $x'$  to  $x$ . It merely assumes that the likelihood decreases exponentially with the distance between the corrupted and clean images. As a result, this approach yields a blind image denoising framework that does not require prior knowledge of the noise type or its magnitude. However, computing the score of this probability distribution is intractable in practice, as it requires evaluating an expectation over the entire ambient space.

## 2.4 Probability and Geometry: The Manifold Hypothesis

One of our main contributions is to introduce in this formulation the manifold hypothesis; namely, we propose that the probability of clean images is concentrated on a low-dimensional manifold

$$P_c(x') = \int P(G(z)) \delta(x' - G(z)) dV_{\mathcal{M}}, \quad (4)$$

where  $z = F(x')$  is the latent representation of the clean image  $x'$ . This means that  $P_c(x') = P(G(z))$  per manifold’s volume unit if  $x' \in \mathcal{M}$  and 0 otherwise. Substituting  $P_c(x')$  in Eq. (3) and after changing the order of integration, we obtain (the derivation is given in Appendix A.1):

$$P_{\text{non-u}}(x; \sigma) = \int_{\mathbb{R}^d} P_\sigma(x | G(z))P(z)dz. \quad (5)$$

Note that  $P_{\text{non-u}}(x; \sigma)$  accounts for the nonuniform distribution of clean images on the manifold, and the integration is performed in the *latent space*. In the limit  $\sigma \rightarrow 0$ , only the point on the manifold closest to  $x$  contributes significantly, and for small enough  $\sigma$ , denoted  $\sigma_d$ , we obtain:

$$P_{\sigma_d}(x | G(z)) \propto P_d(x) := \frac{1}{Q_d} \exp\left(-\frac{\mathcal{D}_{\mathcal{M}}^2(x)}{2\sigma_d^2}\right), \quad (6)$$

where  $Q_d$  is a normalization factor. In this limit, we obtain an “Energy-based model” where  $E = \mathcal{D}_{\mathcal{M}}^2$ . We can ignore the limiting process by which this EBM was derived and postulate it with a variance  $\sigma_d^2$  of our choice. It is worth mentioning that learning directly the distance  $\mathcal{D}_{\mathcal{M}}$  to the manifold makes the algorithm time/noise condition free. This distance encapsulates the noise/time approximation using the actual quantity of interest: the distance to the manifold of clean images. It therefore resolves another challenge associated with using diffusion models for image restoration [28].

## 2.5 Kernel Density Estimation in Latent Space

In the formulation of  $P_{\text{non-u}}(x; \sigma)$  derived above (5),(6), the probability at  $x$  is obtained by integrating contributions from all points on the manifold, where the conditional probability depends solely on the distance to the manifold and is thus purely geometric. Each contribution is weighted by  $P(z)$ , which represents the likelihood that the point  $G(z)$  on the manifold corresponds to a clean image.

Since the distribution  $P(z)$  is unknown, we estimate it using a kernel density method [23, 20], a.k.a. ideal denoiser with delta mixture distribution / empirical distribution [31, 11]:

$$P(z) \approx P_{\text{ker}}(z) := \frac{1}{Q_{\text{ker}}} \sum_{\alpha \in S} \exp\left(-\frac{\|z - z_\alpha\|^2}{2\sigma_{\text{ker}}^2}\right), \quad (7)$$

where  $S$  is the set of latent code indices corresponding to clean images, and  $Q_{\text{ker}}$  is the normalization constant. Note that  $\sigma_{\text{ker}}$  is a hyperparameter that should be chosen carefully.

In Fig. 2, we illustrate  $P_{\text{ker}}(z)$ . Clearly, the encoding of a generic image  $x$  in the latent space, i.e.,  $F(x)$ , may lie in a region with low probability. The probability of a point  $x$  being an image depends on its distance to every point on the manifold, weighted by the probability of that point in the latent space. Using this kernel approximation together with the conditional probability (2), Eq. (5) takes the form

$$P_{\text{non-u}}(x; \sigma_d) \approx \hat{P}_{\text{non-u}}(x; \sigma_d) := \frac{1}{Q_d Q_{\text{ker}}} \sum_{\alpha \in S} \int_{\mathbb{R}^d} \exp\left(-\frac{\|x - G(z)\|^2}{2\sigma_d^2}\right) \exp\left(-\frac{\|z - z_\alpha\|^2}{2\sigma_{\text{ker}}^2}\right) dz. \quad (8)$$

## 3 Geometric View of Diffusion Models

Since both the encoder  $F$  and the manifold distance  $\mathcal{D}_{\mathcal{M}}$  are defined over the ambient space  $\mathbb{R}^D$ , training mappings that induce a diffusion-like flow from corrupted images back to clean manifold samples requires sampling in this high-dimensional space. However, this sampling is inherently difficult due to the curse of dimensionality. Following diffusion models, we obtain ambient samples by adding Gaussian noise to the data points. Although this strategy does not cover all possible corruptions, it empirically yields effective mappings. Notably, despite being trained solely with Gaussian noise, our models generalize well to other types of image corruptions at test time.

To relate a corrupted image to its clean projection, we use the concept of the score. The score is a  $D$ -dimensional vector field defined by  $s(x) = \nabla_x \log P(x)$ , which points in the direction of the steepest ascent of the probability density. For the distance-based probability distribution  $P_d(x)$  (6), we obtain:

$$s_d(x) = \nabla_x \log P_d(x) = \frac{\nabla_x P_d(x)}{P_d(x)} = -\frac{1}{\sigma_d^2} \mathcal{D}_{\mathcal{M}}(x) \nabla_x \mathcal{D}_{\mathcal{M}}(x). \quad (9)$$

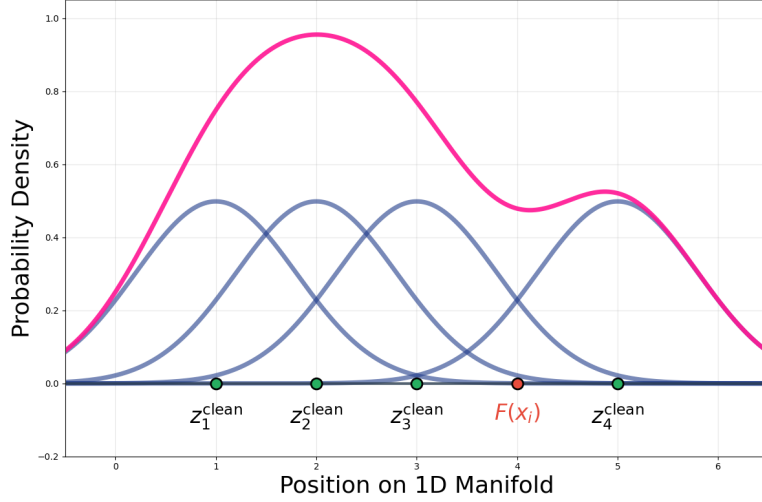


Figure 2: An illustration of the kernel approximation  $P_{\text{ker}}(z)$  of the probability distribution  $P(z)$  in the latent space.

Since  $\mathcal{D}_{\mathcal{M}}(x)$  is the distance to the manifold, its gradient  $\nabla_x \mathcal{D}_{\mathcal{M}}(x)$  is a unit vector pointing to the closest point on the manifold. Therefore, for  $\sigma_d = 1$  we have:

$$x^{\text{shift}} := x + s_d(x) = x - \mathcal{D}_{\mathcal{M}}(x) \nabla_x \mathcal{D}_{\mathcal{M}}(x) = G(F(x)) = x^*, \quad (10)$$

where  $x^*$  is the point on the manifold closest to  $x$  (see Fig. 3).

To incorporate the probability distribution of clean images on the manifold (or equivalently, in the latent space), we interpret the probability in the ambient space as a marginal distribution. This allows the approximation of the score function using a kernel-based method:

$$s(x) = \nabla_x \log P_{\text{non-u}}(x) \approx \nabla_x \log \hat{P}_{\text{non-u}}(x) =: \hat{s}(x).$$

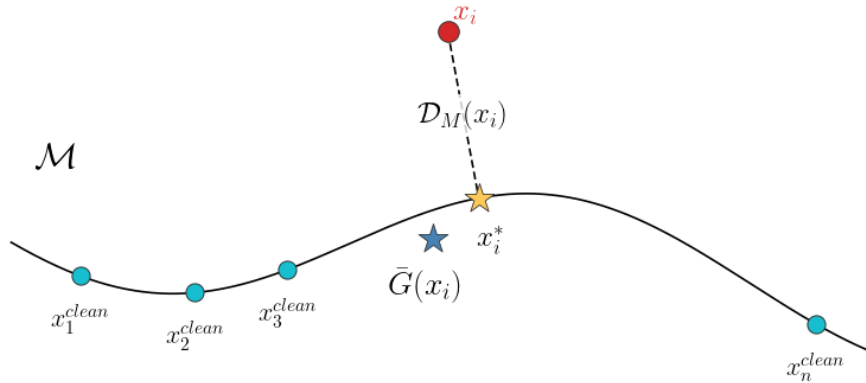


Figure 3: The manifold  $\mathcal{M}$  is illustrated as the curved line.  $x_i^*$  is the closest point to  $x$  on the manifold.  $\bar{G}(x)$  is depicted as well and is not necessarily a point on the manifold.

Direct computation results in

$$\hat{s}(x) = -\frac{1}{2\sigma_d^2} (x - \bar{G}(x)), \quad (11)$$

where  $\bar{G}(x) = \sum_{\alpha \in S} \bar{G}_\alpha(x)$ , and

$$\bar{G}_\alpha(x) = \frac{1}{\hat{P}_{\text{non-u}}(x) Q_{\text{ker}}} \int \left[ G(z) P(x | G(z)) \exp\left(-\frac{\|z - z_\alpha\|^2}{2\sigma_{\text{ker}}^2}\right) \right] dz. \quad (12)$$

Note that  $\bar{G}(x)$ , which is the mean of the contributions from all points on the manifold to the probability  $P_d(x)$  does not necessarily lie on the manifold. In contrast,  $x^* = G(F(x))$  is, by definition, a point on the manifold. See Fig. 3 for an illustration and Fig. 4 for a synthetic example.

Compared to prior work,  $\bar{G}(x)$  in Eq. (11) is the same object as  $\mathbb{E}_{y \in P_c} [y|x]$  in Kadkhodaie et al [10]. This quantity is intractable because the integral can't be approximated by sampling clean images beyond the points in the data set. It is therefore often replaced by the denoiser  $x^*$  [10]. Clearly, the approximation of  $\bar{G}$  by  $x^*$  is justified only under a uniform distribution over the manifold. In contrast, in our geometric formulation the integral over  $z$  in the computation of  $\bar{G}_\alpha(x)$  is approximated by randomly sampling the normal distribution centered around the training point  $z_\alpha$  (for details, see Appendix A.2.).

A noisy or corrupted image  $x$  can be viewed as a point in the ambient space. The image generation then becomes the task of finding an appropriate, though not necessarily orthogonal, projection of this point onto the manifold of clean, meaningful images. If the mappings and functions  $G$ ,  $F$ , and  $\mathcal{D}_M$  are perfectly accurate, a single step can move  $x$  closer to the corresponding clean image. Since the ambient space is sampled sparsely, particularly in regions far from the manifold, the learned approximations become less accurate as the distance from the manifold increases. To mitigate this, we apply multiple iterative steps that progressively refine the estimate as the trajectory approaches the manifold. This procedure resembles a diffusion-like flow; see Fig. 4 for an illustrative example.

Equations (9) and (10) motivate a diffusion-like process guided by the distance function. The score induces a vector field in the ambient space. Using the Tweedie formula [4], we update the sample by taking a step toward the manifold projection, i.e., toward the closest point on the manifold. This yields the iterative update

$$x^{n+1} = x^n - \alpha \mathcal{D}_M(x^n) \hat{\nabla}_x \mathcal{D}_M(x^n) \quad \text{with } 0 < \alpha < 1 \quad \text{and} \quad x^0 = x \quad (13)$$

where

$$\hat{\nabla}_x \mathcal{D}_M(x) := \frac{\nabla_x \mathcal{D}_M(x)}{\|\nabla_x \mathcal{D}_M(x)\|} \quad (14)$$

denotes the normalized gradient of the distance function. Since the distance network provides only an approximation, we normalize the gradient to better control the step size.

Equation (13) does not take into account the distribution of training samples along the manifold. To address this limitation, we incorporate the score induced by the kernel formulation and, by applying Tweedie formula (see Appendix A.3), to obtain

$$x^{n+1} = (1 - \beta)x^n + \beta \bar{G}(x^n) - \alpha \mathcal{D}_M(x^n) \hat{\nabla}_x \mathcal{D}_M(x^n), \quad \text{with } 0 < \alpha, \beta, \alpha + \beta < 1, \quad x^0 = x. \quad (15)$$

The trajectory of  $x$  as it moves toward the manifold is illustrated in Fig. 4.

## 4 Methods

### 4.1 Manifold-Probabilistic Projection Model (MPPM)

The autoencoder and the distance function are implemented as separate neural networks and are jointly trained using the following loss function

$$\begin{aligned} \mathcal{L}(F, G, \mathcal{D}_M) = & \lambda_1 \sum_{x_i \notin \mathcal{M}} (\mathcal{D}_M(x_i) - \|x_i - x_i^*\|)^2 + \lambda_2 \sum_{x_i \in \mathcal{M}} \|x_i^{\text{clean}} - G(F(x_i^{\text{clean}}))\|^2 \\ & + \lambda_3 \sum_{x_i \in \mathcal{M}} |\mathcal{D}_M(x_i)|^2 + \lambda_4 \sum_{x_i \in \mathbb{R}^D} (\mathcal{D}_M(x_i) - |\mathcal{D}_M(x_i)|)^2 + \lambda_5 \sum_{x_i \in \mathbb{R}^D} \|x_i^{\text{shift}} - x_i^*\|^2, \end{aligned} \quad (16)$$

where

$$x_i^{\text{shift}} = x_i - \mathcal{D}_M(x_i) \hat{\nabla}_x \mathcal{D}_M(x_i) \quad (17)$$

and

$$x_i^* = G(F(x_i)). \quad (18)$$

The first term defines the distance function assuming a perfect autoencoder; the second is the standard autoencoder loss. The third term enforces the boundary condition on the distance function and the fourth ensures

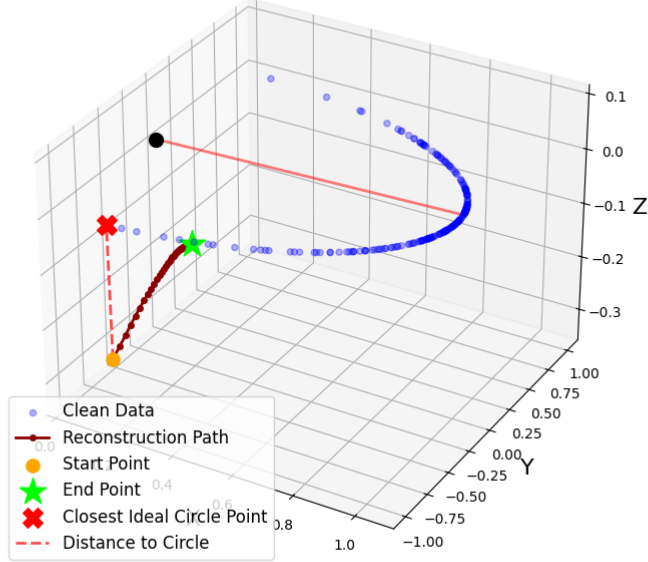


Figure 4: The manifold  $\mathcal{M}$  is the unit circle lying in the xy-plane and is parametrized by the azimuth angle  $\theta$ . It is sampled according to a normal distribution centered at  $\theta_0$  indicated by the red line. The reconstruction trajectory is shown in dark red. Note that the final result of the iterations on  $x$  does not converge to  $x^*$  which is the closest point on the circle. Instead, it is influenced by the data distribution on the manifold through the effect of  $\tilde{G}(x)$ .

its positivity. The last term enforces the geometric consistency of Eq. (10) (see also Fig. 1). At inference, we use the Tweedie formula (15), where

$$\tilde{G}_\alpha(x) \approx \frac{\sum_{z_i \in \mathcal{N}(z_\alpha, \sigma_{\text{ker}}^2)} G(z_i) \exp(-\|x - G(z_i)\|^2 / 2\sigma_d^2)}{\sum_{z_i \in \mathcal{N}(z_\alpha, \sigma_{\text{ker}}^2)} \exp(-\|x - G(z_i)\|^2 / 2\sigma_d^2)} \quad (19)$$

as derived in Appendix A.2.

Algorithm 1 outlines the training procedure using the clean dataset  $\mathcal{X}^{\text{clean}}$  and the reconstruction of a noisy point  $x$  in the ambient space. The algorithm is demonstrated for the simple case of a non-uniform distribution on the circle embedded in  $\mathbb{R}^3$  in Figs. 4 and 5. All the experimental and optimization details can be found in appendices B and C.

---

#### Algorithm 1 MPPM

---

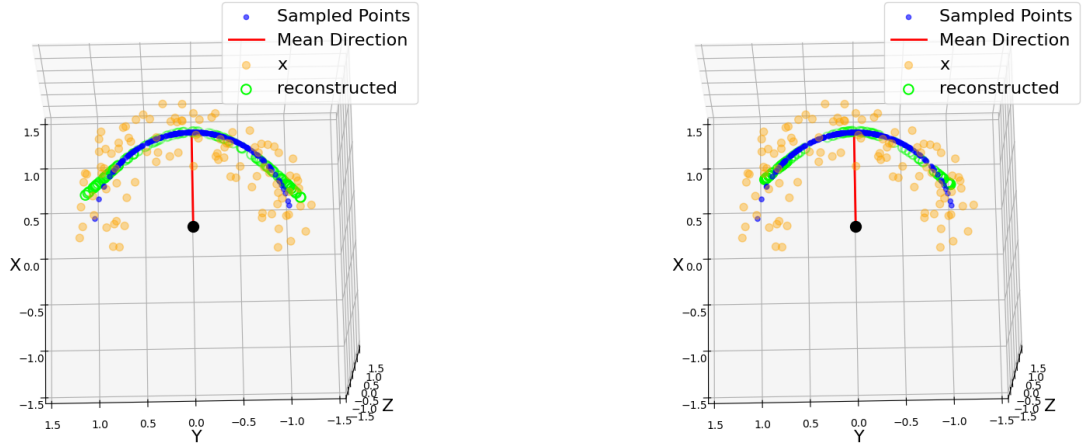
```

function TRAIN( $\mathcal{X}^{\text{clean}}, \epsilon \sim \mathcal{N}(0, \sigma_d^2)$ )
   $G, F, \mathcal{D}_M \leftarrow \text{Train}(\mathcal{X}^{\text{clean}}, \epsilon, \mathcal{L}(F, G, \mathcal{D}_M))$ 
end function
function RECONSTRUCTION( $x, \mathcal{X}^{\text{clean}}, \alpha, \beta, \text{num\_steps}$ )  $\triangleright 0 < \alpha, \beta, \alpha + \beta < 1$ 
   $x^1 \leftarrow x$ 
  for  $n \leftarrow 1$  to num_steps do
     $x^{n+1} \leftarrow (1 - \beta)x^n + \beta \sum_\alpha \tilde{G}_\alpha(x^n) - \alpha \mathcal{D}_M(x^n) \hat{\nabla}_x \mathcal{D}_M(x^n)$  by (15), (19)
  end for
  return  $x^{n+1}$ 
end function

```

---

Figures 6 and 7 illustrate the advantages of the proposed MPPM method compared to the diffusion model. We used 1000 diffusion steps during both training and inference. Because the data points are not uniformly



(a) DAE restoration. MSE = 0.032, max error = 0.147.      (b) MPPM restoration. MSE = 0.026, max error = 0.060.

Figure 5: Comparison between the DAE and our proposed MPPM, this example uses the same setup as in Fig. 4. The error was computed as the deviation from the unit circle in 2D. In regions of the circle with lower probability density, the DAE is more prone to error than the proposed MPPM method.

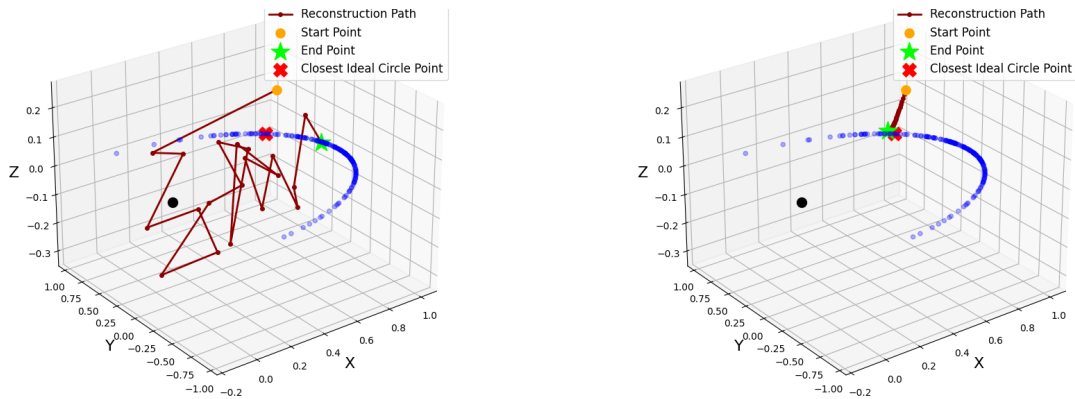


Figure 6: Left: Diffusion model trajectory, Right: MPPM trajectory

distributed, most of the diffusion model’s reconstructed samples concentrate in the dense region (the upper half-circle), as shown in the left panel of Fig. 7. In contrast, the proposed MPPM method effectively handles this non-uniformity through our formulation, resulting in a significantly smaller reconstruction error. Pseudocode for DDPM (Denoising Diffusion Probabilistic Model) training and inference is summarized in Algorithms 2 and 3. Note the difference from Chen et.al. 2024 [2], who analyzed the trajectory of the flow by measuring the deviation from the line between the degraded image and the point found on the manifold.

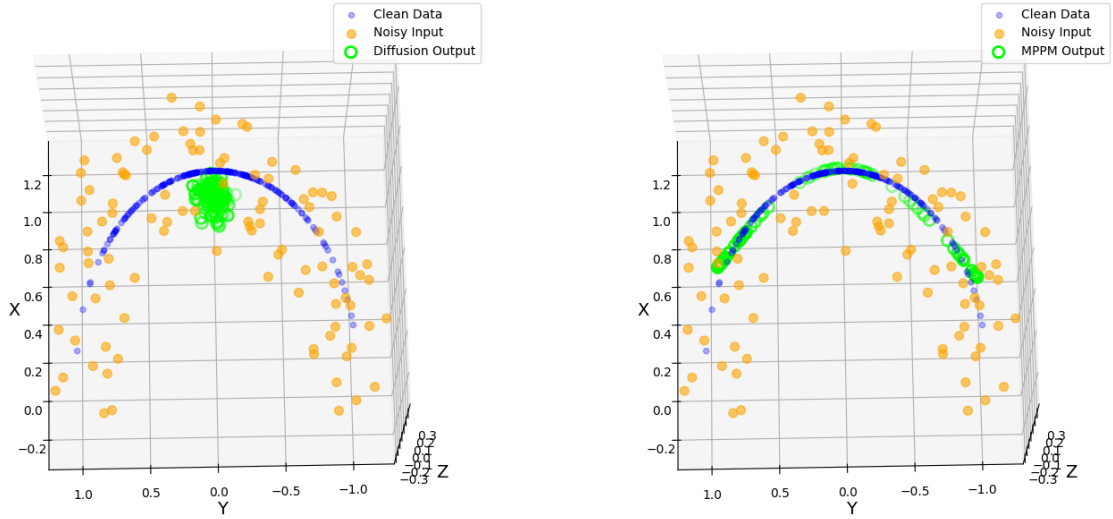


Figure 7: Left: Diffusion restoration, MSE=0.138, Right: MPPM restoration, MSE=0.026

---

### Algorithm 2 DDPM Training

---

- 1: **Precompute noise schedule:**
- 2:  $\beta_t$  (linear schedule from 0.0001 to 0.02)
- 3:  $\alpha_t = 1 - \beta_t$
- 4:  $\bar{\alpha}_t = \prod_{i=1}^t \alpha_i$
- 5: **for each batch do**
- 6:   Sample timestep  $t \sim \text{Uniform}(0, T - 1)$
- 7:   Sample noise  $\epsilon \sim \mathcal{N}(0, I)$
- 8:   **Forward diffusion:**
- 9:   Predict noise:  $\epsilon_{\text{pred}} = \text{model}(x_t, t/T)$
- 10:   Compute loss:
- 11:   Backpropagate and update parameters
- 12: **end for**

$$x_t = \sqrt{\bar{\alpha}_t} x_0 + \sqrt{1 - \bar{\alpha}_t} \epsilon$$

$$L = \|\epsilon - \epsilon_{\text{pred}}\|^2$$

---

### Algorithm 3 DDPM Inference (Stochastic, 1000 steps)

---

- 1: Initialize  $x_T \sim \mathcal{N}(0, I)$
  - 2: **for**  $t = T - 1$  **down to** 0 **do**
  - 3:   Predict noise:  $\epsilon_{\text{pred}} = \text{model}(x_t, t/T)$
  - 4:   **Denoise:**
  - 5:   **if**  $t > 0$  **then**
  - 6:     Sample  $z \sim \mathcal{N}(0, I)$
  - 7:     Add noise:  $x_t = x_t + \sigma_t z$
  - 8:   **end if**
  - 9: **end for**
  - 10: **return**  $x_0$
- 

$$x_t = \frac{x_t - \text{coef}_t \epsilon_{\text{pred}}}{\sqrt{\alpha_t}}$$

## 4.2 Latent MPPM (LMPPM)

The key difference between the pixel space and the latent space is that, in the latter, we do not assume that encoded clean and meaningful images lie on a lower-dimensional manifold. Instead, we treat the set of encoded clean and meaningful images as a point cloud that occupies the full dimension of the latent space. We model this set as samples from a probability distribution  $P(z)$ . Let the set of clean and meaningful images be  $\mathcal{X}^{\text{clean}}$  and the set of these encoded images be  $S = \{F(\mathcal{X}^{\text{clean}})\}$ . In this context,  $S$  serves the role that the manifold  $\mathcal{M}$  played in the previous section, in the sense that the distance function  $\mathcal{D}_S$  is now computed *in the latent space* with respect to the set  $S$ . Let  $x \in \mathbb{R}^D$  be an image and  $z = F(x) \in \mathbb{R}^d$  its latent representation. The reconstructed image is then given by  $\hat{x} = G(z)$ . Let us define a distance function  $\mathcal{D}_S : \mathbb{R}^d \rightarrow \mathbb{R}$  such that  $\mathcal{D}_S(z)$  measures the distance from  $z$  to the set  $S$  in the latent space. Using this, we define a shift in the latent space as:  $z^{\text{shift}} := z - \mathcal{D}_S(z)\hat{\nabla}_z \mathcal{D}_S(z)$ . The loss function is then given by

$$\begin{aligned} \mathcal{L}(F, G, \mathcal{D}_S) = & \lambda_1 \sum_{z_i \notin S} (\mathcal{D}_S(z_i) - \|z_i - z_i^*\|)^2 + \lambda_2 \sum_{z_i \in S} \|x_i^{\text{clean}} - G(z_i)\|^2 \\ & \lambda_3 \sum_{z_i \in S} |\mathcal{D}_S(z_i)|^2 + \lambda_4 \sum_{z_i} (\mathcal{D}_S(z_i) - |\mathcal{D}_S(z_i)|)^2 \\ & + \lambda_5 \sum_{z_i \notin S} \|z_i^{\text{shift}} - z_i^*\| + \lambda_6 \sum_{z_i \notin S} \|G(z_i^{\text{shift}}) - x_i^*\|, \end{aligned} \quad (20)$$

where  $x_i^* = \arg \min_{\tilde{x} \in \mathcal{X}^{\text{clean}}} \|x_i - \tilde{x}\|$ , and  $z_i^* = F(x_i^*)$ . These definitions ensure that a generic point  $x$  in the ambient space, whose closest clean image in the dataset is  $x^*$  is mapped to  $z = F(x)$  such that its nearest neighbor in  $S$  is  $z^* = F(x^*)$ . It is important to note that the set  $S$  evolves over training iterations as the encoder  $F$  and decoder  $G$  are updated, and the distance function  $\mathcal{D}_S$  is adjusted accordingly. The first three terms are the heart of the algorithm. The 4th element ensures positivity. The 5th and 6th terms improve consistency between all three networks. Ablation study empirically proves that these terms contribute to the performance of the method. By the kernel method,  $\bar{G}(x)$  is replaced by

$$\bar{z} = \frac{1}{Q} \sum_{x_j \in \mathcal{X}} F(x_j) \exp\left(-\frac{(z - F(x_j))^2}{2\sigma_{ker}^2}\right). \quad (21)$$

The complete procedure is described in Algorithm 4.

---

### Algorithm 4 LMPPM

---

```

function TRAIN( $\mathcal{X}^{\text{clean}}, \epsilon \sim \mathcal{N}(0, \sigma_d^2)$ )
   $G, F, \mathcal{D}_S \leftarrow \text{Train}(\mathcal{X}^{\text{clean}}, \epsilon, \mathcal{L}(F, G, \mathcal{D}_S))$   by (20)
end function
function RECONSTRUCTION( $x, \mathcal{X}^{\text{clean}}, \alpha, \beta, \text{num\_steps}$ )
   $z^1 \leftarrow F(x)$ 
  for  $n \leftarrow 1$  to  $\text{num\_steps}$  do
     $z^{n+1} \leftarrow (1 - \beta)z^n + \beta\bar{z}^n - \alpha\mathcal{D}_S(z^n)\hat{\nabla}_z \mathcal{D}_S(z^n)$   by (21)
  end for
  return  $G(z^{n+1})$ 
end function

```

---

## 5 Experiments

We evaluated our MPPM method on synthetic data and our LMPPM method on real-world image datasets, where we simultaneously trained an autoencoder-like network for  $F$  and  $G$ , and a different network for the distance function  $\mathcal{D}_{\mathcal{M}}$  and  $\mathcal{D}_S$ . It is important to note that training was performed exclusively with Gaussian noise degradation, while at inference time we evaluated the models under a variety of other degradation types. We compared our results with standard denoising autoencoders (DAE) [29] and latent diffusion models (LDM) [22]. For synthetic experiments, we evaluated on a one-dimensional manifold: a half-circle lying in the xy plane and embedded in  $\mathbb{R}^3$ . The points in the circle are sampled according to angular coordinates drawn from truncated normal distributions (see Figs. 4 and 5).

For real-world data, we experiment with MNIST [13], SCUT-FBP5500 facial beauty dataset [14], and CelebA-HQ-256[16]. To evaluate restoration performance, we apply three types of degradation to MNIST: Gaussian noise, downsampling (super-resolution), and elastic deformation, each at two severity levels. For SCUT-FBP5500 and CelebA-HQ-256, we consider four types of degradation: Gaussian noise, downsampling, random scribbles, and black patches (inpainting), also applied at two severity levels.

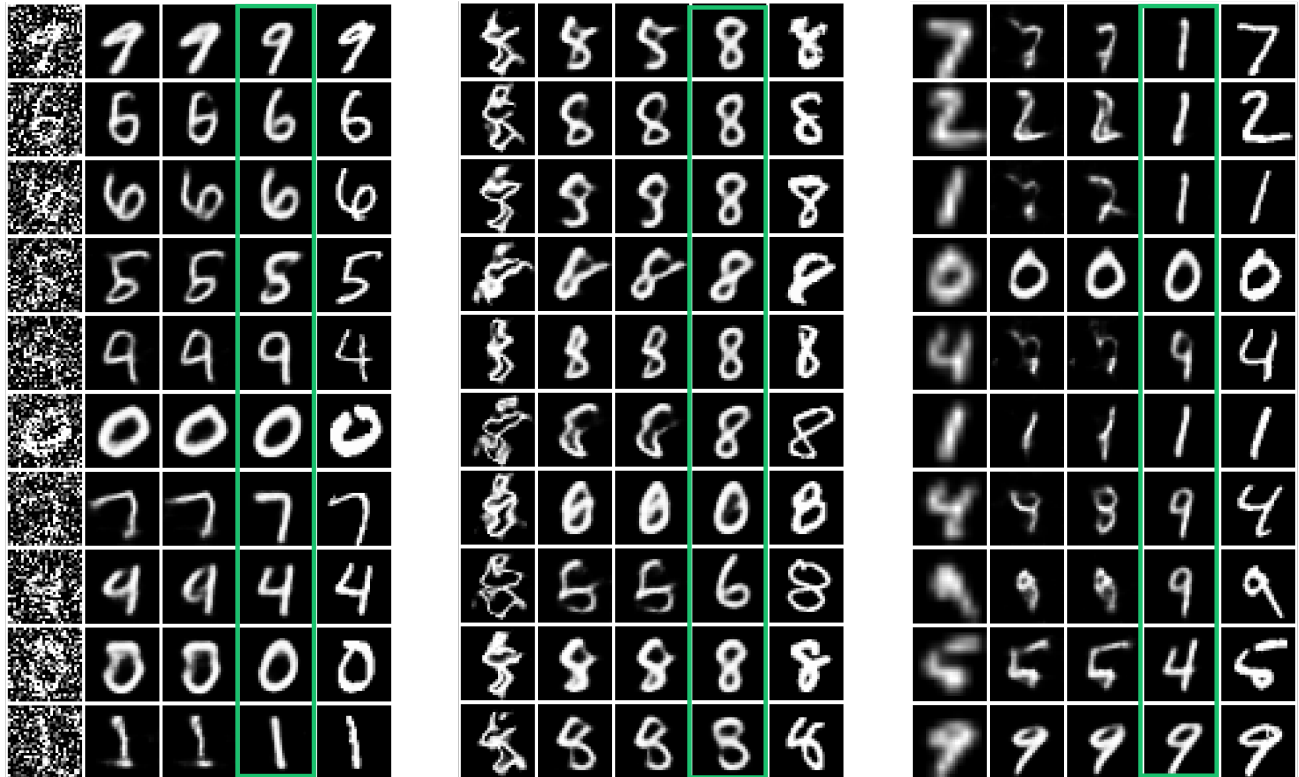


Figure 8: Left panel: noise  $\sigma = 0.7$ ; middle panel: elastic ( $\alpha = 0.34$ ,  $\sigma = 1.8$ ); right panel: downsampling factor = 0.35. In all panels, from left to right: degraded, DAE, LDA, LMMPPM (ours), and original.

We trained our proposed methods and the comparison baselines to assess their performance in the different datasets. Detailed architecture specifications and hyperparameters are provided in appendices B and C. For synthetic data, we implement MPPM using MLP architectures. For MNIST, we employ a CNN-based autoencoder for both DAE and our LMPPM method, while for SCUT-FBP5500 and CelebA-HQ-256 we adopt a U-Net architecture with skip connections. In addition, we construct an extra set of skip connections from the latent space and combine them with the original skips through weighted summation (see Appendix B). The distance functions  $\mathcal{D}_{\mathcal{M}}$  and  $\mathcal{D}_{\mathcal{S}}$  are implemented as MLPs with progressively decreasing layer sizes to perform dimensionality reduction. For LDM, we integrate the corresponding DAE backbone (in place of the autoencoder) with a standard diffusion model, using 2000 diffusion steps.

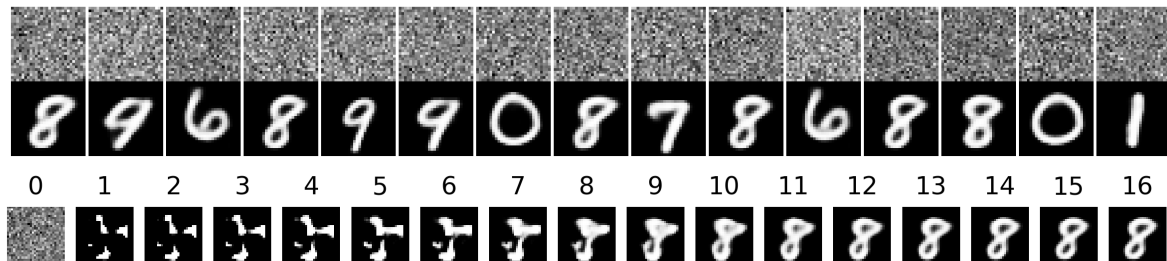


Figure 9: Top: Digit generation from pure noise, with an FID of 19.53 computed over 2000 images. Bottom: Progression of digit generation over 16 steps.

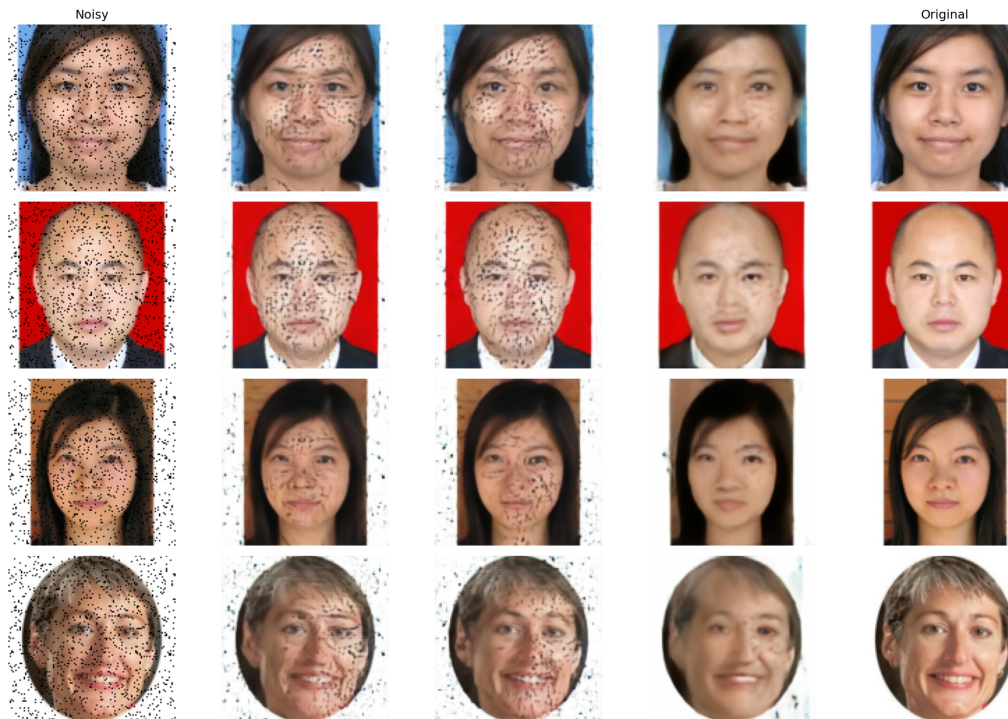


Figure 10: Missing pixels (0.08). From left to right: degraded, DAE, Diffusion, LMPPM, original.

## 5.1 Results

**MNIST results:** For the MNIST dataset, we set the latent space dimension to 18 and the additive noise to  $\epsilon = 0.4$ . To calculate FID, we trained an MNIST classifier and computed an embedding distribution for each class. After reconstructing a degraded digit, we classified it and compared its embedding with the corresponding pre-computed class distribution. Table 1 reports the mean SSIM and FID metrics. Our method consistently outperforms both DAE and LDM baselines across all degradation types in terms of FID scores. Notably, DAE occasionally achieved higher SSIM values, although its visual results were inferior. We additionally performed an ablation study to assess the significance of the distance network. Ablation<sup>lmppm</sup> corresponds to setting  $\alpha = 0$  in the reconstruction process, while Ablation<sup>dae</sup> uses the DAE network instead of our  $(F, G)$  network, also with  $\alpha = 0$ . As can be seen, when using the proposed network (trained with  $\mathcal{D}$ ), the results improve compared to the DAE variant, but still remain below the performance of the full reconstruction setting ( $\alpha > 0$ ).

Fig. 8 illustrates restoration examples for Gaussian noise, elastic deformation, and downsampling. Additional experiment included the generation of digits from a pure noise. We generated 200 images from random Gaussian noise and managed to obtain realistic digits (FID=19.5) as can be seen in Fig. 9.

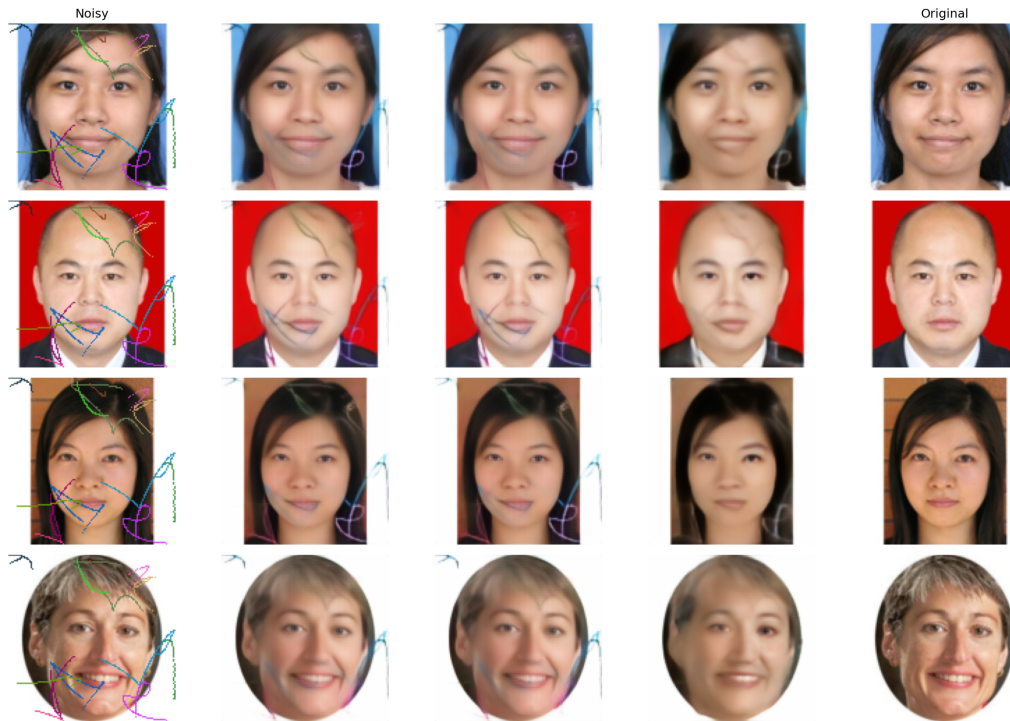


Figure 11: Images with 13 scribbles. From left to right: degraded, DAE, Diffusion, LMPPM, original.

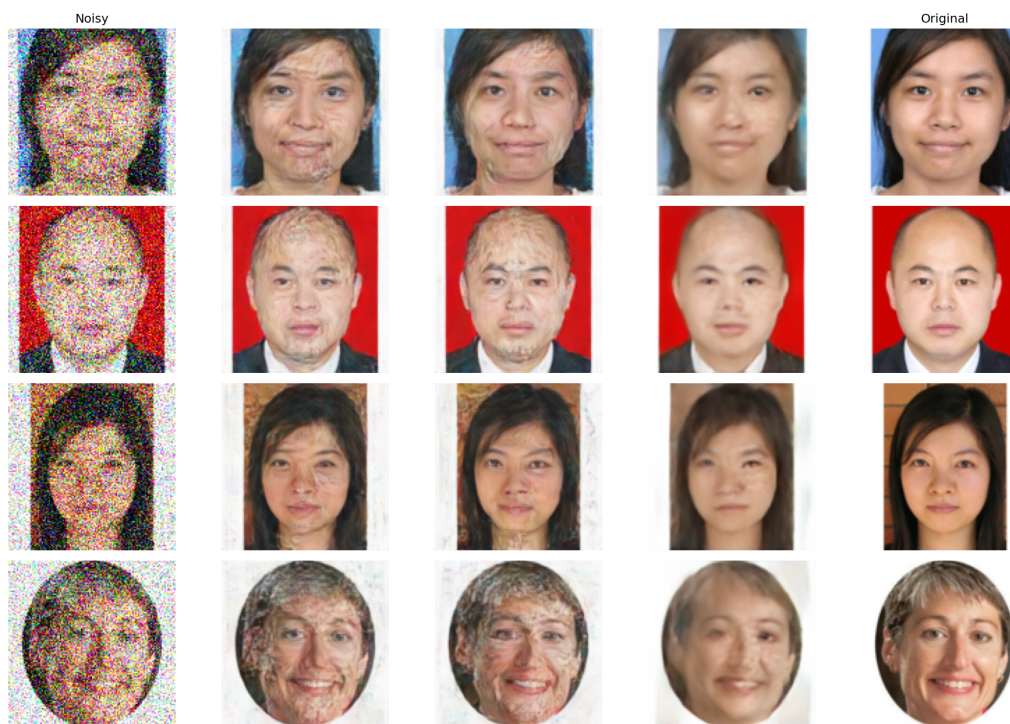


Figure 12: Noise  $\sigma = 0.3$ . From left to right: degraded, DAE, Diffusion, LMPPM, original.

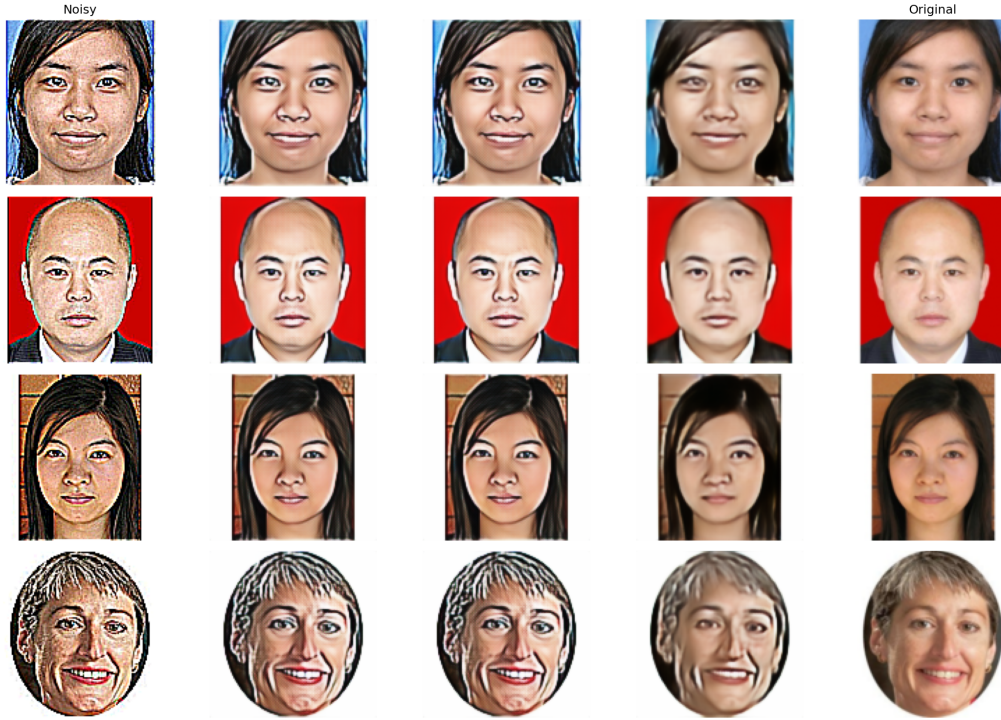


Figure 13: Over sharpening (18). From left to right: degraded, DAE, LDM, LMPPM, original.



Figure 14: Gradual reconstruction of missing pixels (0.08) degradation.

Table 1: Quantitative results on MNIST

	Elastic 2.3		Elastic 1.8	
	SSIM $\uparrow$	FID $\downarrow$	SSIM $\uparrow$	FID $\downarrow$
DAE	<u>0.66</u>	69.36	<u>0.59</u>	134.60
LDM	0.64	66.52	0.58	124.05
LMPPM (ours)	0.63	<b>12.61</b>	<u>0.59</u>	<b>16.38</b>
Ablation <sup>lmppm</sup>	0.63	12.83	0.59	16.27
Ablation <sup>dae</sup>	0.17	522.39	0.15	527.25
	Downsample 0.5		Downsample 0.35	
	SSIM $\uparrow$	FID $\downarrow$	SSIM $\uparrow$	FID $\downarrow$
DAE	<u>0.79</u>	31.66	<u>0.54</u>	133.66
LDM	0.75	31.61	0.53	128.80
LMPPM (ours)	0.67	<b>11.27</b>	0.52	<b>22.65</b>
Ablation <sup>lmppm</sup>	0.67	11.34	0.52	22.89
Ablation <sup>dae</sup>	0.17	521.14	0.13	504.08

Table 2: Quantitative results on SCUT-FBP5500

	Noise 0.2		Noise 0.25		Noise 0.3	
	SSIM	FID	SSIM	FID	SSIM	FID
DAE	<u>0.928</u>	21.78	<u>0.904</u>	27.15	0.828	42.52
LDM	0.925	<b>13.00</b>	0.901	18.68	0.822	34.19
LMPPM (ours)	0.868	14.95	0.888	<b>17.07</b>	<u>0.839</u>	<b>21.35</b>
	Miss pixels 0.04		Miss pixels 0.08		Miss pixels 0.1	
	SSIM $\uparrow$	FID $\downarrow$	SSIM $\uparrow$	FID $\downarrow$	SSIM $\uparrow$	FID $\downarrow$
DAE	<u>0.917</u>	33.90	0.798	49.00	0.745	47.94
LDM	0.914	27.35	0.798	41.47	0.738	44.41
LMPPM (ours)	0.881	<b>16.20</b>	<u>0.862</u>	<b>23.92</b>	<u>0.832</u>	<b>34.13</b>
	Scribble 6		Scribble 13		Scribble 20	
	SSIM $\uparrow$	FID $\downarrow$	SSIM $\uparrow$	FID $\downarrow$	SSIM $\uparrow$	FID $\downarrow$
DAE	<u>0.921</u>	34.83	<u>0.889</u>	45.66	0.860	51.68
LDM	0.919	29.31	0.887	39.02	0.859	44.66
LMPPM (ours)	0.879	<b>16.73</b>	0.878	<b>17.35</b>	<u>0.869</u>	<b>18.46</b>
	Sharpen 8		Sharpen 10		Sharpen 18	
	SSIM $\uparrow$	FID $\downarrow$	SSIM $\uparrow$	FID $\downarrow$	SSIM $\uparrow$	FID $\downarrow$
DAE	<u>0.902</u>	28.53	<u>0.883</u>	29.80	0.815	33.82
LDM	0.898	20.79	0.878	21.73	0.807	25.37
LMPPM (ours)	0.878	<b>16.79</b>	0.874	<b>17.33</b>	<u>0.853</u>	<b>19.48</b>



Figure 15: Left to right: over-sharpened input, DAE, LDM, LMPPM (ours), and original. LMPPM remains realistic despite changes to the face.

**SCUT-FBP5500 Results:** Figs. 10, 11, 12, and 13 present restoration results in facial images under different types of degradation: random missing pixels, random scribbles, strong Gaussian noise, and over sharpening. The quantitative evaluation in Table 2 supports these visual findings, with our method consistently achieving lower FID scores in all degradation scenarios. For these experiments, we set the latent dimension at 1024 and the additive noise at  $\epsilon = 0.2$ . Although the DAE baseline achieves higher SSIM values in certain cases, the perceptual fidelity of its reconstructions remains inferior to that of our approach. Fig. 14 illustrates the reconstruction after four iterations. Finally, in Fig. 15, although the reconstructed face differs slightly from the original, our method yields a result that exhibits higher perceptual realism and lies closer to the natural face manifold, while alternative methods produce reconstructions with a more artificial appearance.

**CelebA Dataset result** We evaluate our method on the CelebA-HQ-256 dataset, adopting the same architecture used for SCUT-FBP5500. The qualitative and quantitative results are presented in Figs. 16 and 17, and Table 3. Our approach achieves a markedly lower FID score, while maintaining SSIM values comparable to the competing methods.

We further compared our method to DiffBIR [15]. DiffBIR tackles blind image restoration using two stages: degradation removal and information regeneration. The first stage removes degradations and produces a high-fidelity but often over-smoothed intermediate result, while the second stage regenerates realistic textures and details. For completeness, we conducted three experiments: (i) DiffBIR after its first stage only, (ii) full DiffBIR, and (iii) our LMPPM followed by DiffBIR’s second stage. The results are shown in Fig. 18 and in the bottom panel of Table 3.

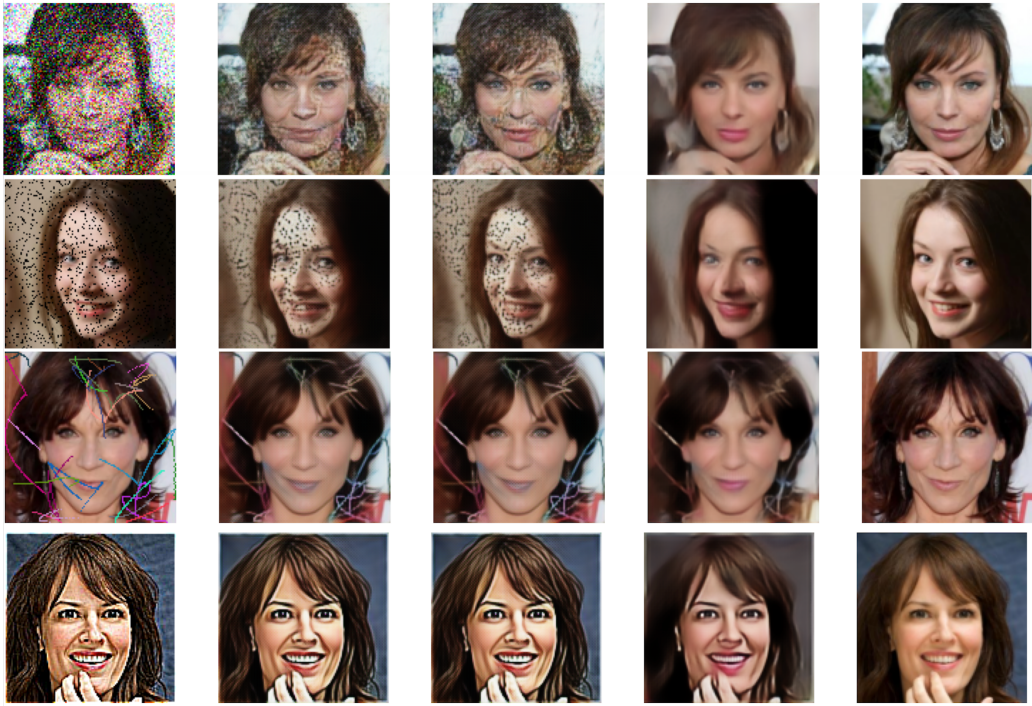


Figure 16: Different degradations applied to the CelebA-HQ-256 dataset. From top to bottom: noise ( $\sigma = 0.3$ ), missing pixels (0.1), scribbles (22), over sharpening (12). From left to right: degraded, DAE, LDM, LMPPM (ours), and original.

As can be seen, LMPPM outperforms the first stage of DiffBIR both visually (second and third columns from the left) and quantitatively, especially under the missing-pixel and scribble degradations. The output of DiffBIR’s second stage is realistic and perceptually high-quality. Notably, the full DiffBIR model (fourth column from the left of Fig. 18) performs well in removing Gaussian noise (first row), even though the reconstructed image differs from the original image (right column). The best performance is achieved by applying our LMPPM followed by DiffBIR’s second stage (second column from the right), indicating that our blind degradation-removal module provides a strong foundation for high-quality restoration.

## 6 Summary and Conclusions

This work emphasizes the *Manifold Hypothesis* and interprets established image restoration and generation methods through a novel geometric perspective. Beyond presenting a unifying framework, which is valuable in its own right, we propose incorporating a learned distance function to the manifold. By leveraging distances to the



Figure 17: Excessive Gaussian noise ( $\sigma = 0.3$ ) applied on CelebA-HQ-256 dataset. From left to right: degraded, DAE, LDM, LMPPM and original.

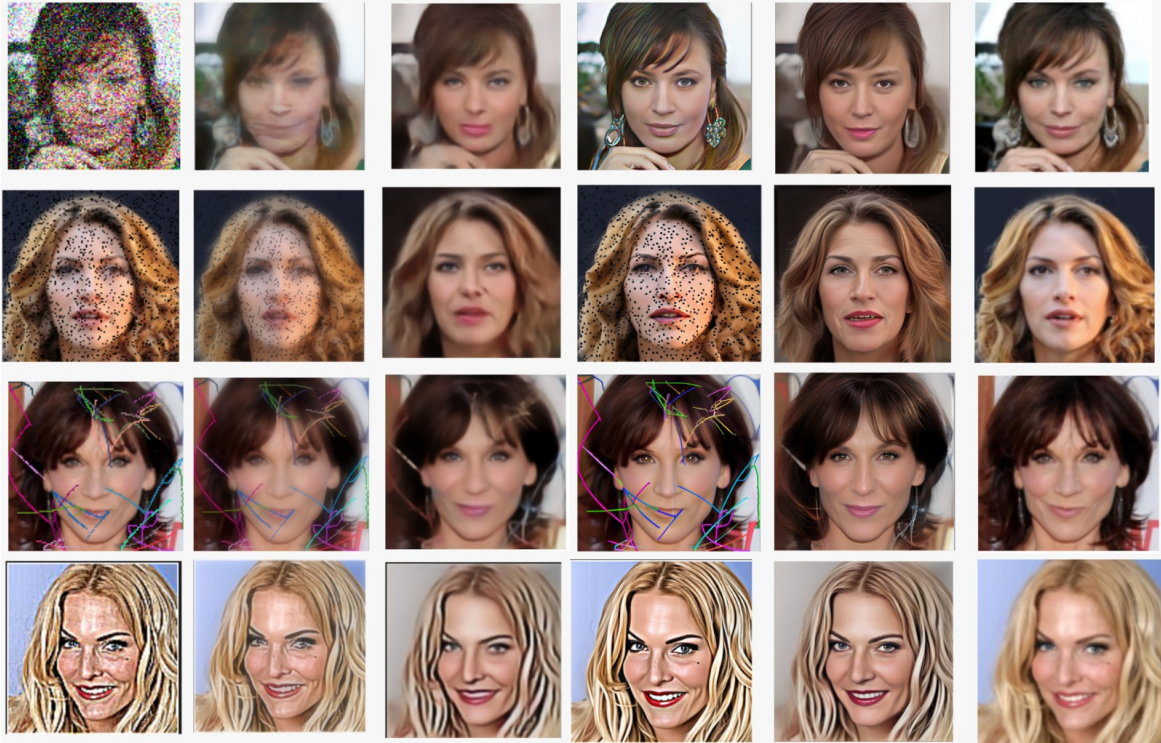


Figure 18: Comparison to DiffBIR method [15]. From top to bottom: noise ( $\sigma = 0.3$ ), missing pixels (0.1), scribbles (22), over sharpening (12). From left to right: degraded, DiffBIR stage1, LMPPM, DiffBIR (stage1 + stage2), LMPPM+DiffBIR stage2, original

Table 3: Quantitative results on the CelebA-HQ-256 dataset, compared also to the DiffBIR method [15].

	Noise 0.3		Scribbles 22		Miss Pixels 0.1		Sharpen 12	
	SSIM $\uparrow$	FID $\downarrow$						
DAE	0.694	43.05	<u>0.817</u>	54.75	<u>0.762</u>	49.23	0.719	46.64
LDM	0.663	34.99	0.793	42.73	0.757	41.38	<u>0.724</u>	34.54
LMPPM (ours)	<u>0.707</u>	<b>23.92</b>	0.757	<b>30.69</b>	0.671	<b>25.63</b>	0.714	<b>28.25</b>
DiffBIR	<u>0.70</u>	24.09	0.69	42.95	0.58	42.52	0.76	31.95
DiffBIR stage1	0.67	28.52	<u>0.71</u>	43.85	<u>0.69</u>	44.01	<u>0.89</u>	28.55
LMPPM+DiffBIR stage2	0.68	<b>22.64</b>	0.69	<b>30.68</b>	0.63	<b>23.21</b>	0.72	<b>25.69</b>

manifold, we establish a connection between the geometric structure and a probability density approximation. By employing a kernel-like method to approximate the probability distribution on the manifold, or equivalently on the latent space, we integrate geometry and probability in a novel manner. We induce a vector field in the ambient space via the score of these probability densities. This vector field directs each point toward the manifold of clean images, considering both the structure and the distribution of clean and meaningful images on the manifold.

In this work, we utilize a (denoising) autoencoder in conjunction with the distance function. Providing an approach where both  $F$  and  $G$  define the manifold while maintaining their coupling to the distance function  $\mathcal{D}$  from it. However, due to potential errors in the outputs of the three networks  $G$ ,  $F$  and  $\mathcal{D}$ , especially when  $x$  is far from the manifold, this vector field is not exact. Therefore, rather than applying a single-step (weighted) projection onto the manifold, we proceed iteratively, advancing in small steps along the noisy vector field. We are currently exploring an analogous approach where VAE and GAN are coupled with the distance function. A key practical advantage of our approach is that it operates in latent space. This dimensionality reduction substantially improves the accuracy of the learned distance function, which in turn enhances both restoration and generation performance. Indeed, as demonstrated in Section 5.1, comparisons with leading baselines show that our method consistently outperforms competing approaches, particularly under severe distortions across

multiple datasets and degradation types.

## Acknowledgments

We gratefully acknowledge Prof. Yoel Shkolnisky and Prof. Haim Avron for fruitful discussions in the early stages of the project as part of the department research group. We also thank Prof. Yoel Shkolnisky and Dr. Dmitry Batenkov for generously providing unrestricted access to their computational infrastructure, including GPU servers, which were essential for this research.

## References

- [1] Clément Chadebec and Stéphanie Allasonnière. A geometric perspective on variational autoencoders. In *Advances in Neural Information Processing Systems*, 2022.
- [2] D. Chen, Z. Zhou, C. Wang, C. Shen, and S Lyu. On the trajectory regularity of ode-based diffusion sampling, 2024.
- [3] Tim R. Davidson, Luca Falorsi, Nicola De Cao, Thomas Kipf, and Jakub M. Tomczak. Hyperspherical variational auto-encoders, 2022.
- [4] B. Efron. Tweedie’s formula and selection bias. 106(496):1602–1614, 2011.
- [5] Mevlana C Gemici, Danilo Jimenez Rezende, and Shakir Mohamed. Normalizing flows on Riemannian manifolds. In *NeurIPS Workshop on Bayesian Deep Learning*, 2016.
- [6] Ian Goodfellow, Jean Pouget-Abadie, Mehdi Mirza, Bing Xu, David Warde-Farley, Sherjil Ozair, Aaron Courville, and Yoshua Bengio. Generative adversarial nets. In *Advances in Neural Information Processing Systems*, 2014.
- [7] William Rowan Hamilton. Theory of systems of rays. 15:69–174, 1828.
- [8] Jonathan Ho, Ajay Jain, and Pieter Abbeel. Denoising diffusion probabilistic models. In *Advances in Neural Information Processing Systems*, 2020.
- [9] Jonathan Ho, Ajay Jain, and Pieter Abbeel. Denoising diffusion probabilistic models. In *Advances in Neural Information Processing Systems*, 2020.
- [10] Z. Kadkhodaie, F. Guth, E. P. Simoncelli, and S. Mallat. Generalization in diffusion models arises from geometry-adaptive harmonic representations, 2023.
- [11] T. Karras, M. Aittala, T. Aila, and S. Laine. Elucidating the design space of diffusion-based generative models. In *Proceedings of the 35th Advances in Neural Information Processing Systems*, pages 26565–26577, 2020.
- [12] Diederik P Kingma and Max Welling. Auto-encoding variational bayes, 2013.
- [13] Yann LeCun. The mnist database of handwritten digits. <http://yann.lecun.com/exdb/mnist/>, 1998.
- [14] Lingyu Liang, LuoJun Lin, Lianwen Jin, Duorui Xie, and Mengru Li. Scut-fbp5500: A diverse benchmark dataset for multi-paradigm facial beauty prediction. 2018.
- [15] Xinqi Lin, Jingwen He, Ziyang Chen, Zhaoyang Lyu, Bo Dai, Fanghua Yu, Yu Qiao, Wanli Ouyang, and Chao Dong. Diffbir: Towards blind image restoration with generative diffusion prior. In *Proceedings of the European Conference on Computer Vision (ECCV)*, volume 15117 of *Lecture Notes in Computer Science*, pages 430–448. Springer, 2024.
- [16] Ziwei Liu, Ping Luo, Xiaogang Wang, and Xiaoou Tang. Deep learning face attributes in the wild. In *Proceedings of International Conference on Computer Vision (ICCV)*, December 2015.
- [17] Gabriel Loaiza-Ganem, Brendan Leigh Ross, Rasa Hosseinzadeh, Anthony L. Caterini, and Jesse C. Cresswell. Deep generative models through the lens of the manifold hypothesis: A survey and new connections, 2024.

- [18] Emile Mathieu, Charline Le Lan, Chris J. Maddison, Ryota Tomioka, and Yee Whye Teh. Continuous hierarchical representations with poincaré variational auto-encoders, 2019.
- [19] Emile Mathieu and Maximilian Nickel. Riemannian continuous normalizing flows. In *Advances in Neural Information Processing Systems*, 2020.
- [20] E. Parzen. On estimation of a probability density function and mode. 33(3):1065–1076, 1962.
- [21] Danilo Jimenez Rezende and Shakir Mohamed. Variational inference with normalizing flows. In *International Conference on Machine Learning*, 2015.
- [22] Robin Rombach, Andreas Blattmann, Dominik Lorenz, Patrick Esser, and Björn Ommer. High-resolution image synthesis with latent diffusion models. In *Proceedings of the IEEE/CVF Conference on Computer Vision and Pattern Recognition (CVPR)*, 2022.
- [23] M. Rosenblatt. Remarks on some nonparametric estimates of a density function. 27(3):832–837, 1956.
- [24] David E. Rumelhart and James L. McClelland. *Learning Internal Representations by Error Propagation*, pages 318–362. 1987.
- [25] H. Shao, A. Kumar, and P. Thomas Fletcher. The riemannian geometry of deep generative models. In *Proceedings Proceedings of the IEEE Conference on Computer Vision and Pattern Recognition Workshops*, pages 15–323, 2018.
- [26] Jascha Sohl-Dickstein, Eric A. Weiss, Niru Maheswaranathan, and Surya Ganguli. Deep unsupervised learning using nonequilibrium thermodynamics, 2015.
- [27] Yang Song and Stefano Ermon. Generative modeling by estimating gradients of the data distribution, 2020.
- [28] Q. Sun, Z. Jiang, H. Zhao, and K. He. Is noise conditioning necessary for denoising generative models?, 2025.
- [29] Pascal Vincent, Hugo Larochelle, Yoshua Bengio, and Pierre-Antoine Manzagol. Extracting and composing robust features with denoising autoencoders. In *Proceedings of the 25th international conference on Machine learning*, pages 1096–1103, 2008.
- [30] B. Wang and C. R. Ponce. The geometry of deep generative image models and its applications, 2021.
- [31] J. J. Wang, B. and Vastola. The unreasonable effectiveness of gaussian score approximation for diffusion models and its applications, 2024.

# A Detailed Theory

## A.1 Manifold Likelihood Derivation

Here we derive Eq. (5). Let  $x$  denote a general point in the ambient space, and let  $x'$  be a clean data point. We denote the probability density of clean images by  $P_c(x')$ . Then,

$$\begin{aligned} P_{\text{non-u}}(x) &= \int_{\mathcal{M}} P(x, x') dx' = \int_{\mathbb{R}^D} P(x | x') P_c(x') dx' \\ &= \int_{\mathbb{R}^D} P(x | x') \left( \int_{\mathcal{M}} P(G(z)) \delta(x' - G(z)) dV_{\mathcal{M}} \right) dx' \\ &= \int_{\mathcal{M}} P(x | x' = G(z)) P(G(z)) \underbrace{\sqrt{g} dz}_{dV_{\mathcal{M}}} = \int_{\mathbb{R}^d} P(x | G(z)) P(z) dz. \end{aligned}$$

Here  $dV_{\mathcal{M}} = \sqrt{g} dz$  is the manifold's volume element, where  $g = \det G$  and  $G_{\mu\nu} = \sum_{i=1}^D J_{\mu}^i J_{\nu}^i$  is the induced metric, with the Jacobian of the embedding map given by  $J_{\mu}^i = \partial G^i(z) / \partial z_{\mu}$ . In the last equality, we use the identity  $P(G(z)) = P(z)(\sqrt{g})^{-1}$ .

## A.2 Score Function

Recall the score function

$$s(x) = \nabla_x \log P_{\text{non-u}}(x) \approx \nabla_x \log \hat{P}_{\text{non-u}}(x) =: \hat{s}(x).$$

Direct computation results in

$$\hat{s}(x) = -\frac{1}{2\sigma_d^2} (x - \bar{G}(x)), \quad (22)$$

where  $\bar{G}(x) = \sum_{\alpha \in S} \bar{G}_{\alpha}(x)$ , and

$$\bar{G}_{\alpha}(x) = \frac{1}{\hat{P}_{\text{non-u}}(x) Q_{\text{ker}}} \int \left[ G(z) P(x | G(z)) \exp\left(-\frac{\|z - z_{\alpha}\|^2}{2\sigma_{\text{ker}}^2}\right) \right] dz. \quad (23)$$

We approximate the integral over  $z$  in (23) for  $\bar{G}_{\alpha}(x)$  by Monte Carlo sampling from the normal distribution centered at the training point  $z_{\alpha}$ . Specifically, we estimate the mean by averaging over  $n$  samples.

$$\int \left[ G(z) P(x | G(z)) \exp\left(-\frac{\|z - z_{\alpha}\|^2}{2\sigma_{\text{ker}}^2}\right) \right] dz \approx \frac{1}{Q_d} \frac{1}{n} \sum_{z_i \in \mathcal{N}(z_{\alpha}, \sigma_{\text{ker}}^2)} G(z_i) \exp\left(-\frac{\|x - G(z_i)\|^2}{2\sigma_d^2}\right), \quad (24)$$

where  $\alpha$  denotes an index in the training set. The calculation of  $\bar{G}_{\alpha}(x)$  requires evaluating  $\hat{P}_{\text{non-u}}(x)$  in the denominator. In particular, by (8)

$$\hat{P}_{\text{non-u}} = \frac{1}{Q_{\text{ker}}} \int \left[ P(x | G(z)) \exp\left(-\frac{\|z - z_{\alpha}\|^2}{2\sigma_{\text{ker}}^2}\right) \right] dz \approx \frac{1}{Q_{\text{ker}} Q_d} \frac{1}{n} \sum_{z_i \in \mathcal{N}(z_{\alpha}, \sigma_{\text{ker}}^2)} \exp\left(-\frac{\|x - G(z_i)\|^2}{2\sigma_d^2}\right). \quad (25)$$

Substituting (24) and (25) in (23) yields

$$\bar{G}_{\alpha}(x) \approx \frac{\sum_{z_i \in \mathcal{N}(z_{\alpha}, \sigma_{\text{ker}}^2)} G(z_i) \exp(-\|x - G(z_i)\|^2 / 2\sigma_d^2)}{\sum_{z_i \in \mathcal{N}(z_{\alpha}, \sigma_{\text{ker}}^2)} \exp(-\|x - G(z_i)\|^2 / 2\sigma_d^2)}. \quad (26)$$

Note that all constant factors  $Q_d$ ,  $Q_{\text{ker}}$  and  $\frac{1}{n}$ , are canceled between the numerator and the denominator.

## A.3 The Tweedie Formula

The ‘‘flow’’ equations (13) and (15) are the Tweedie formulas for the corresponding probability functions where (13) follows

$$P_d(x) = \frac{1}{Q_d} \exp\left(-\frac{\alpha}{2} \mathcal{D}_{\mathcal{M}}^2(x)\right), \quad (27)$$

and (15) follows

$$P(x) = \frac{1}{Z} P_d(x) \sum_{\alpha \in S} \int_{\mathbb{R}^d} \exp\left(-\frac{\beta}{2} \|x - G(z)\|^2\right) \exp\left(-\frac{\|z - z_\alpha\|^2}{2\sigma_{\text{ker}}^2}\right) dz, \quad (28)$$

where  $Z$  is a normalization factor. One can easily verify from (13) that we decrease the distance to the manifold along the flow. Indeed,

$$\begin{aligned} \mathcal{D}_{\mathcal{M}}(x^{n+1}) &= \mathcal{D}_{\mathcal{M}}(x^n - \epsilon \mathcal{D}_{\mathcal{M}}(x^n) \nabla_x \mathcal{D}_{\mathcal{M}}(x^n)) \\ &= \mathcal{D}_{\mathcal{M}}(x^n) - \epsilon \nabla \mathcal{D}_{\mathcal{M}}(x^n) \cdot \mathcal{D}_{\mathcal{M}}(x^n) \nabla_x \mathcal{D}_{\mathcal{M}}(x^n) + O(\epsilon^2) = (1 - \epsilon) \mathcal{D}_{\mathcal{M}}(x^n) + O(\epsilon^2), \end{aligned}$$

where we used the fact that the distance function is a solution of the Eikonal equation  $\|\nabla_x \mathcal{D}_{\mathcal{M}}(x)\|^2 = 1$ .

## B Detailed Experimental Setup

### B.1 Notation and Abbreviations

In the following tables we summarize the abbreviations and datasets through the paper.

Table 4: Glossary of abbreviations and terms used throughout the paper

Term	Definition
DAE	Denoising Autoencoder
MPPM	Manifold Projection and Propagation Method (our proposed approach)
LMPPM	Latent Manifold Projection and Propagation Method (our proposed approach)
LDM	Latent Diffusion Model
SSIM	Structural Similarity Index Measure
BN	Batch Normalization

Table 5: Summary of experimental datasets used for evaluating restoration performance

Dataset	Description
MNIST	60,000 training/10,000 test grayscale images ( $28 \times 28$ pixels)
SCUT-FBP5500	5,500 facial images with beauty scores (resized to $120 \times 120$ )
CelebA-HQ-256	30,000 high-quality celebrity face images ( $256 \times 256$ )

### B.2 Degradations

**Degradation Parameters** We apply six degradation types to simulate real-world image corruption scenarios. Each degradation is applied at two severity levels (intermediate, and severe) to test the robustness of restoration methods.

**Degradation Methods** Brief descriptions of each degradation type:

- **Gaussian noise:** Additive zero-mean Gaussian noise that simulates sensor noise or transmission errors.
- **Elastic deformation:** Non-rigid distortions implemented using `torchvision.transform.ElasticTransform( $\alpha = 34, \sigma$ )` that simulate warping effects.
- **Super-resolution:** Downsampling followed by upsampling to original resolution, simulating reconstruction from low-resolution data.
- **Missing Pixels:** Set black patches with some coverage portion
- **Scribbles:** Add  $n$  random scribbles with random colors
- **Over Sharpening by factor  $s$ :**  $I = I + s(I - I * \sigma_s)$

Table 6: Degradation parameters at different severity levels. Note: Lower  $\sigma$  values for elastic deformation indicate more severe distortion due to increased localized displacement

Degradation	Mild	Severe
Gaussian noise ( $\sigma$ ) MNIST	0.7	0.85
Gaussian noise ( $\sigma$ ) Faces	0.2	0.3
Elastic deformation ( $\sigma$ )	2.3	1.8
Super-resolution (downsampling factor)	0.5	0.35
Missing Pixels	0.04	0.1
Number of Scribbles	6	22
Over Sharpening	8	18

### B.3 Model Architectures

We implemented three main architectures across all experiments, with design choices tailored to each dataset’s complexity.

**Synthetic Data Model** Synthetic data for MPPM experiments use MLP-based networks with a latent dimension of 1, selected based on the low intrinsic dimensionality of this manifold:

Table 7: Network architectures for synthetic data experiments. All models use fully-connected layers

Component	Architecture
Encoder	3 $\rightarrow$ 64 $\rightarrow$ 64 $\rightarrow$ 1 with ReLU
Decoder	1 $\rightarrow$ 64 $\rightarrow$ 64 $\rightarrow$ 3 with ReLU
Distance Network	3 $\rightarrow$ 16 $\rightarrow$ 8 $\rightarrow$ 4 $\rightarrow$ 1 with ReLU

**MNIST Models** MNIST experiments use CNN-based models with latent dimension 18, chosen to capture the variability among handwritten digits while promoting compact representations.

Table 8: Network architectures for MNIST experiments

Component	Architecture
Encoder	Conv2d(1 $\rightarrow$ 32 $\rightarrow$ 64, kernel = 3, stride = 2) $\rightarrow$ Flatten $\rightarrow$ Linear(64 $\times$ 7 $\times$ 7 $\rightarrow$ 18)
Decoder	Linear(18 $\rightarrow$ 64 $\times$ 7 $\times$ 7) $\rightarrow$ Reshape $\rightarrow$ ConvTranspose2d(64 $\rightarrow$ 32 $\rightarrow$ 1) $\rightarrow$ Sigmoid
Distance Network	18 $\rightarrow$ 100 $\rightarrow$ 50 $\rightarrow$ 20 $\rightarrow$ 1 with ReLU, dropout=0.2

**SCUT-FBP5500 and CelebA-HQ-256 Models** Facial image experiments employ a U-Net with skip connections and a latent dimension of 1024, which accommodates the higher complexity of facial features while enabling detailed reconstruction. Facial image experiments employ a U-Net with skip connections and a latent dimension of 1024, which accommodates the higher complexity of facial features while enabling detailed reconstruction. Note that in the U-Net architecture, during the inference process we use iterations (denoted by superscripts) such that

$$F(x^n) = (S_1^n, S_2^n, \dots, S_k^n, z^n)^T,$$

and

$$x^{n+1} = G\left(S_1^n + \hat{S}_1^n(z^{n+1}), S_2^n + \hat{S}_2^n(z^{n+1}), \dots, S_k^n + \hat{S}_k^n(z^{n+1}), z^{n+1}\right).$$

Here, each  $\hat{S}_i^n(z^{n+1})$  denotes the projection of the latent space  $z^{n+1}$  onto the corresponding skip connection  $S_i^n$ . Thus, the updated skip connection is formed by adding the original skip feature  $S_i^n$  with the new projected feature  $\hat{S}_i^n(z^{n+1})$  before being passed to  $G$ . The architecture is illustrated in Fig. 19.

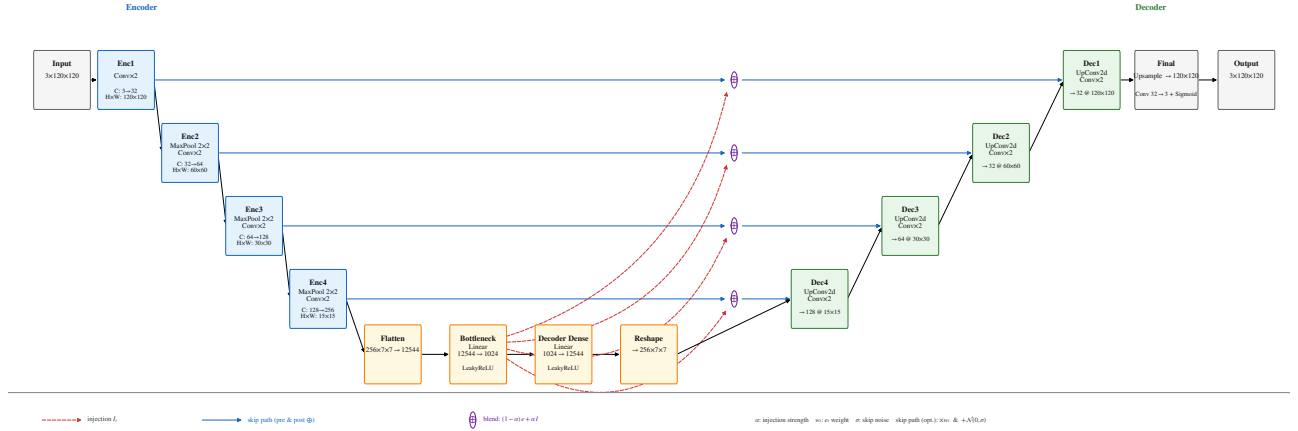


Figure 19: Modified U-net architecture

Table 9: Network architectures for SCUT-FBP5500 and CelebA-HQ-256 experiments. Skip connections connect corresponding Encoder and Decoder layers through concatenation. The encoder and decoder blocks are represented as parameterized functions (shown in italic font), where  $C_{in}$ ,  $C_{out}$ , and  $C_{skip}$  represent the number of input, output, and skip connection channels respectively. Abbreviations: Conv = Conv2d (kernel=3, padding=1), BN = BatchNorm2d, LReLU = LeakyReLU(0.2), MPool = MaxPool2d(2), ConvT = ConvTranspose2d(kernel=2, stride=2), Cat = Concatenation. The bottleneck dimension is 1024.

Component	Structure
EncoderBlock( $C_{in} \rightarrow C_{out}$ )	Conv( $C_{in} \rightarrow C_{out}$ ) $\rightarrow$ BN $\rightarrow$ LReLU $\rightarrow$ Conv( $C_{out} \rightarrow C_{out}$ ) $\rightarrow$ BN $\rightarrow$ LReLU $\rightarrow$ MPool
Encoder	EncoderBlock(3 $\rightarrow$ 32), output: $60 \times 60$ EncoderBlock(32 $\rightarrow$ 64), output: $30 \times 30$ EncoderBlock(64 $\rightarrow$ 128), output: $15 \times 15$ EncoderBlock(128 $\rightarrow$ 256), output: $7 \times 7$ Flatten $\rightarrow$ Linear(12544 $\rightarrow$ 1024) $\rightarrow$ LReLU
DecoderBlock( $C_{in}, C_{skip}, C_{out}$ )	ConvT( $C_{in} \rightarrow C_{in}$ ) $\rightarrow$ Cat( $[C_{in}, C_{skip}]$ ) $\rightarrow$ Conv( $C_{in} + C_{skip} \rightarrow C_{in}$ ) $\rightarrow$ BN $\rightarrow$ LReLU $\rightarrow$ Conv( $C_{in} \rightarrow C_{out}$ ) $\rightarrow$ BN $\rightarrow$ LReLU
Decoder	Linear(1024 $\rightarrow$ 12544) $\rightarrow$ Reshape(256, 7, 7) DecoderBlock(256, 256, 128), output: $15 \times 15$ DecoderBlock(128, 128, 64), output: $30 \times 30$ DecoderBlock(64, 64, 32), output: $60 \times 60$ DecoderBlock(32, 32, 32), output: $120 \times 120$ Conv(32 $\rightarrow$ 3) $\rightarrow$ Sigmoid
Distance Network	1024 $\rightarrow$ 300 $\rightarrow$ 100 $\rightarrow$ 30 $\rightarrow$ 1 with ReLU, dropout=0.2

## C Training and Evaluation

Table 10: MPPM training and inference parameters for synthetic data

Parameter	Value
Optimizer	Adam ( $\beta_1 = 0.9, \beta_2 = 0.999$ )
Learning rates	AE: $1 \times 10^{-3}$ , Distance network: $1 \times 10^{-3}$
Weight decay	$1 \times 10^{-4}$
Batch size	550
Training epochs	1500
Loss function	Composite loss (Equation 16)
Early stopping	Patience: 100
$\alpha$ (distance gradient step)	0.15
$\beta$ (kernel averaging weight)	0.1
Convergence tolerance	0.005
Maximum iterations	60

Table 11: LMPPM training parameters across all experiments, determined through preliminary grid search, diffusion steps are define the number of steps in algorithm 4

Parameter	Value
Optimizer	Adam ( $\beta_1 = 0.9, \beta_2 = 0.999$ )
Learning rates	AE: $1 \times 10^{-3}$ , Distance network: $1 \times 10^{-3}$ (MNIST $1 \times 10^{-5}$ ), LDM: $1 \times 10^{-3}$
Batch size	MNIST: 128, SCUT-FBP5500: 32
Training epochs	MNIST: 200, SCUT-FBP5500: 75
Loss functions	DAE: L2, LDM: MSE, LMPPM: Composite loss 20
Early stopping	Patience: 10 epochs
Diffusion steps	MNIST: 2000, SCUT-FBP5500: 2000